

This work was written as part of one of the author's official duties as an Employee of the United States Government and is therefore a work of the United States Government. In accordance with 17 U.S.C. 105, no copyright protection is available for such works under U.S. Law. Access to this work was provided by the University of Maryland, Baltimore County (UMBC) ScholarWorks@UMBC digital repository on the Maryland Shared Open Access (MD-SOAR) platform.

Please provide feedback

Please support the ScholarWorks@UMBC repository by emailing scholarworks-group@umbc.edu and telling us what having access to this work means to you and why it's important to you. Thank you.

FERMI LARGE AREA TELESCOPE VIEW OF THE CORE OF THE RADIO GALAXY CENTAURUS A

A. A. ABDO^{1,2}, M. ACKERMANN³, M. AJELLO³, W. B. ATWOOD⁴, L. BALDINI⁵, J. BALLE⁶, G. BARBIELLINI^{7,8}, D. BASTIERI^{9,10}, B. M. BAUGHMAN¹¹, K. BECHTOL³, R. BELLAZZINI⁵, B. BERENJI³, R. D. BLANDFORD³, E. D. BLOOM³, E. BONAMENTE^{12,13}, A. W. BORGLAND³, A. BOUVIER³, T. J. BRANDT^{11,14}, J. BREGEON⁵, A. BREZ⁵, M. BRIGIDA^{15,16}, P. BRUEL¹⁷, R. BUEHLER³, S. BUSON^{9,10}, G. A. CALIANDRO¹⁸, R. A. CAMERON³, A. CANNON^{19,20}, P. A. CARAVEO²¹, S. CARRIGAN¹⁰, J. M. CASANDJIAN⁶, E. CAVAZZUTI²², C. CECCHI^{12,13}, Ö. ÇELİK^{19,23,24}, E. CHARLES³, A. CHEKHTMAN^{1,25}, C. C. CHEUNG^{1,2}, J. CHIANG³, S. CIPRINI¹³, R. CLAUS³, J. COHEN-TANUGI²⁶, S. COLAFRANCESCO²², L. R. COMINSKY²⁷, J. CONRAD^{28,29,68}, L. COSTAMANTE³, D. S. DAVIS^{19,24}, C. D. DERMER¹, A. DE ANGELIS³⁰, F. DE PALMA^{15,16}, E. DO COUTO E SILVA³, P. S. DRELL³, R. DUBOIS³, D. DUMORA^{31,32}, A. FALCONE³³, C. FARNIER²⁶, C. FAVUZZI^{15,16}, S. J. FEGAN¹⁷, J. FINKE^{1,2}, W. B. FOCKE³, P. FORTIN¹⁷, M. FRAILIS^{30,34}, Y. FUKAZAWA³⁵, S. FUNK³, P. FUSCO^{15,16}, F. GARGANO¹⁶, D. GASPARRINI²², N. GEHRELS¹⁹, M. GEORGANOPOULOS²⁴, S. GERMANI^{12,13}, B. GIEBELS¹⁷, N. GIGLIETTO^{15,16}, P. GIOMMI²², F. GIORDANO^{15,16}, M. GIROLETTI³⁶, T. GLANZMAN³, G. GODFREY³, P. GRANDI³⁷, I. A. GRENIER⁶, M.-H. GRONDIN^{31,32}, J. E. GROVE¹, L. GUILLEMOT^{31,32,38}, S. GUIRIEC³⁹, D. HADASCH⁴⁰, A. K. HARDING¹⁹, HAYO HASE⁴¹, M. HAYASHIDA³, E. HAYS¹⁹, D. HORAN¹⁷, R. E. HUGHES¹¹, R. ITOH³⁵, M. S. JACKSON^{29,42}, G. JÓHANNESSEN³, A. S. JOHNSON³, T. J. JOHNSON^{19,43}, W. N. JOHNSON¹, M. KADLER^{23,44,45,46}, T. KAMAE³, H. KATAGIRI³⁵, J. KATAOKA⁴⁷, N. KAWAI^{48,49}, T. KISHISHITA⁵⁰, J. KNÖDLSER¹⁴, M. KUSS⁵, J. LANDE³, L. LATRONICO⁵, S.-H. LEE³, M. LEMOINE-GOUMARD^{31,32}, M. LENA GARDE^{28,29}, F. LONGO^{7,8}, F. LOPARCO^{15,16}, B. LOTT^{31,32}, M. N. LOVELLETTE¹, P. LUBRANO^{12,13}, A. MAKEEV^{1,25}, M. N. MAZZIOTTA¹⁶, W. MCCONVILLE^{19,43}, J. E. MCENERY^{19,43}, P. F. MICHELSON³, W. MITTHUMSIRI³, T. MIZUNO³⁵, A. A. MOISEEV^{23,43}, C. MONTE^{15,16}, M. E. MONZANI³, A. MORSELLI⁵¹, I. V. MOSKALENKO³, S. MURCIA³, C. MÜLLER⁴⁴, T. NAKAMORI⁴⁷, M. NAUMANN-GODO⁶, P. L. NOLAN³, J. P. NORRIS⁵², E. NUSS²⁶, M. OHNO⁵⁰, T. OHSUGI⁵³, R. OJHA⁵⁴, A. OKUMURA⁵⁰, N. OMODEI³, E. ORLANDO⁵⁵, J. F. ORMES⁵², M. OZAKI⁵⁰, C. PAGANI⁵⁶, D. PANEQUE³, J. H. PANETTA³, D. PARENT^{1,25}, V. PELASSA²⁶, M. PEPE^{12,13}, M. PESCE-ROLLINS⁵, F. PIRON²⁶, C. PLÖTZ⁵⁷, T. A. PORTER³, S. RAINÒ^{15,16}, R. RANDO^{9,10}, M. RAZZANO⁵, S. RAZZAQUE^{1,2}, A. REIMER^{3,58}, O. REIMER^{3,58}, T. REPOSEUR^{31,32}, J. RIPKEN^{28,29}, S. RITZ⁴, A. Y. RODRIGUEZ¹⁸, M. ROTH⁵⁹, F. RYDE^{29,42}, H. F.-W. SADROZINSKI⁴, D. SANCHEZ¹⁷, A. SANDER¹¹, J. D. SCARGLE⁶⁰, C. SGRÒ⁵, E. J. SISKIND⁶¹, P. D. SMITH¹¹, G. SPANDRE⁵, P. SPINELLI^{15,16}, J.-L. STARCK⁶, L. STAWARZ^{50,62}, M. S. STRICKMAN¹, D. J. SUSON⁶³, H. TAJIMA³, H. TAKAHASHI⁵³, T. TAKAHASHI⁵⁰, T. TANAKA³, J. B. THAYER³, J. G. THAYER³, D. J. THOMPSON¹⁹, L. TIBALDO^{6,9,10,69}, D. F. TORRES^{18,40}, G. TOSTI^{12,13}, A. TRAMACERE^{3,64,65}, Y. UCHIYAMA³, T. L. USHER³, J. VANDENBROUCKE³, V. VASILEIOU^{23,24}, N. VILCHEZ¹⁴, V. VITALE^{51,66}, A. P. WAITE³, P. WANG³, B. L. WINER¹¹, K. S. WOOD¹, Z. YANG^{28,29}, T. YLINEN^{29,42,67}, AND M. ZIEGLER⁴

¹ Space Science Division, Naval Research Laboratory, Washington, DC 20375, USA; justin.finke@nrl.navy.mil

² National Research Council Research Associate, National Academy of Sciences, Washington, DC 20001, USA

³ W. W. Hansen Experimental Physics Laboratory, Kavli Institute for Particle Astrophysics and Cosmology, Department of Physics and SLAC National Accelerator Laboratory, Stanford University, Stanford, CA 94305, USA

⁴ Santa Cruz Institute for Particle Physics, Department of Physics and Department of Astronomy and Astrophysics, University of California at Santa Cruz, Santa Cruz, CA 95064, USA

⁵ Istituto Nazionale di Fisica Nucleare, Sezione di Pisa, I-56127 Pisa, Italy

⁶ Laboratoire AIM, CEA-IRFU/CNRS/Université Paris Diderot, Service d'Astrophysique, CEA Saclay, 91191 Gif sur Yvette, France

⁷ Istituto Nazionale di Fisica Nucleare, Sezione di Trieste, I-34127 Trieste, Italy

⁸ Dipartimento di Fisica, Università di Trieste, I-34127 Trieste, Italy

⁹ Istituto Nazionale di Fisica Nucleare, Sezione di Padova, I-35131 Padova, Italy

¹⁰ Dipartimento di Fisica "G. Galilei," Università di Padova, I-35131 Padova, Italy

¹¹ Department of Physics, Center for Cosmology and Astro-Particle Physics, The Ohio State University, Columbus, OH 43210, USA

¹² Istituto Nazionale di Fisica Nucleare, Sezione di Perugia, I-06123 Perugia, Italy

¹³ Dipartimento di Fisica, Università degli Studi di Perugia, I-06123 Perugia, Italy

¹⁴ Centre d'Étude Spatiale des Rayonnements, CNRS/UPS, BP 44346, F-30128 Toulouse Cedex 4, France

¹⁵ Dipartimento di Fisica "M. Merlin" dell'Università e del Politecnico di Bari, I-70126 Bari, Italy

¹⁶ Istituto Nazionale di Fisica Nucleare, Sezione di Bari, 70126 Bari, Italy

¹⁷ Laboratoire Leprince-Ringuet, École polytechnique, CNRS/IN2P3, Palaiseau, France

¹⁸ Institut de Ciències de l'Espai (IEEC-CSIC), Campus UAB, 08193 Barcelona, Spain

¹⁹ NASA Goddard Space Flight Center, Greenbelt, MD 20771, USA

²⁰ University College Dublin, Belfield, Dublin 4, Ireland

²¹ INAF-Istituto di Astrofisica Spaziale e Fisica Cosmica, I-20133 Milano, Italy

²² Agenzia Spaziale Italiana (ASI) Science Data Center, I-00044 Frascati (Roma), Italy

²³ Center for Research and Exploration in Space Science and Technology (CRESST) and NASA Goddard Space Flight Center, Greenbelt, MD 20771, USA

²⁴ Department of Physics and Center for Space Sciences and Technology, University of Maryland Baltimore County, Baltimore, MD 21250, USA

²⁵ George Mason University, Fairfax, VA 22030, USA

²⁶ Laboratoire de Physique Théorique et Astroparticules, Université Montpellier 2, CNRS/IN2P3, Montpellier, France

²⁷ Department of Physics and Astronomy, Sonoma State University, Rohnert Park, CA 94928-3609, USA

²⁸ Department of Physics, Stockholm University, AlbaNova, SE-106 91 Stockholm, Sweden

²⁹ The Oskar Klein Centre for Cosmoparticle Physics, AlbaNova, SE-106 91 Stockholm, Sweden

³⁰ Dipartimento di Fisica, Università di Udine and Istituto Nazionale di Fisica Nucleare, Sezione di Trieste, Gruppo Collegato di Udine, I-33100 Udine, Italy

³¹ CNRS/IN2P3, Centre d'Études Nucléaires Bordeaux Gradignan, UMR 5797, Gradignan, 33175, France

³² Université de Bordeaux, Centre d'Études Nucléaires Bordeaux Gradignan, UMR 5797, Gradignan, 33175, France

³³ Department of Astronomy and Astrophysics, Pennsylvania State University, University Park, PA 16802, USA

³⁴ Osservatorio Astronomico di Trieste, Istituto Nazionale di Astrofisica, I-34143 Trieste, Italy

- ³⁵ Department of Physical Sciences, Hiroshima University, Higashi-Hiroshima, Hiroshima 739-8526, Japan; fukazawa@hep01.hepl.hiroshima-u.ac.jp
- ³⁶ INAF Istituto di Radioastronomia, 40129 Bologna, Italy
- ³⁷ INAF-IASF Bologna, 40129 Bologna, Italy
- ³⁸ Max-Planck-Institut für Radioastronomie, Auf dem Hügel 69, 53121 Bonn, Germany
- ³⁹ Center for Space Plasma and Aeronomic Research (CSPAR), University of Alabama in Huntsville, Huntsville, AL 35899, USA
- ⁴⁰ Institució Catalana de Recerca i Estudis Avançats (ICREA), Barcelona, Spain
- ⁴¹ Bundesamt für Kartographie und Geodäsie, Concepción, Chile
- ⁴² Department of Physics, Royal Institute of Technology (KTH), AlbaNova, SE-106 91 Stockholm, Sweden
- ⁴³ Department of Physics and Department of Astronomy, University of Maryland, College Park, MD 20742, USA
- ⁴⁴ Dr. Remeis-Sternwarte Bamberg, Sternwartstrasse 7, D-96049 Bamberg, Germany
- ⁴⁵ Erlangen Centre for Astroparticle Physics, D-91058 Erlangen, Germany
- ⁴⁶ Universities Space Research Association (USRA), Columbia, MD 21044, USA
- ⁴⁷ Research Institute for Science and Engineering, Waseda University, 3-4-1, Okubo, Shinjuku, Tokyo, 169-8555 Japan
- ⁴⁸ Department of Physics, Tokyo Institute of Technology, Meguro City, Tokyo 152-8551, Japan
- ⁴⁹ Cosmic Radiation Laboratory, Institute of Physical and Chemical Research (RIKEN), Wako, Saitama 351-0198, Japan
- ⁵⁰ Institute of Space and Astronautical Science, JAXA, 3-1-1 Yoshinodai, Sagamihara, Kanagawa 229-8510, Japan
- ⁵¹ Istituto Nazionale di Fisica Nucleare, Sezione di Roma “Tor Vergata,” I-00133 Roma, Italy
- ⁵² Department of Physics and Astronomy, University of Denver, Denver, CO 80208, USA
- ⁵³ Hiroshima Astrophysical Science Center, Hiroshima University, Higashi-Hiroshima, Hiroshima 739-8526, Japan
- ⁵⁴ U. S. Naval Observatory, Washington, DC 20392, USA
- ⁵⁵ Max-Planck Institut für extraterrestrische Physik, 85748 Garching, Germany
- ⁵⁶ Department of Physics and Astronomy, University of Leicester, Leicester, LE1 7RH, UK
- ⁵⁷ Bundesamt für Kartographie und Geodäsie, GARS O’Higgins, Antarctica
- ⁵⁸ Institut für Astro- und Teilchenphysik and Institut für Theoretische Physik, Leopold-Franzens-Universität Innsbruck, A-6020 Innsbruck, Austria
- ⁵⁹ Department of Physics, University of Washington, Seattle, WA 98195-1560, USA
- ⁶⁰ Space Sciences Division, NASA Ames Research Center, Moffett Field, CA 94035-1000, USA
- ⁶¹ NYCB Real-Time Computing Inc., Lattingtown, NY 11560-1025, USA
- ⁶² Astronomical Observatory, Jagiellonian University, 30-244 Kraków, Poland
- ⁶³ Department of Chemistry and Physics, Purdue University Calumet, Hammond, IN 46323-2094, USA
- ⁶⁴ Consorzio Interuniversitario per la Fisica Spaziale (CIFS), I-10133 Torino, Italy
- ⁶⁵ INTEGRAL Science Data Centre, CH-1290 Versoix, Switzerland
- ⁶⁶ Dipartimento di Fisica, Università di Roma “Tor Vergata,” I-00133 Roma, Italy
- ⁶⁷ School of Pure and Applied Natural Sciences, University of Kalmar, SE-391 82 Kalmar, Sweden

Received 2010 April 16; accepted 2010 June 27; published 2010 July 29

ABSTRACT

We present γ -ray observations with the Large Area Telescope (LAT) on board the *Fermi Gamma-Ray Space Telescope* of the nearby radio galaxy Centaurus A (Cen A). The previous EGRET detection is confirmed, and the localization is improved using data from the first 10 months of *Fermi* science operation. In previous work, we presented the detection of the lobes by the LAT; in this work, we concentrate on the γ -ray core of Cen A. Flux levels as seen by the LAT are not significantly different from that found by EGRET, nor is the extremely soft LAT spectrum ($\Gamma = 2.67 \pm 0.10_{\text{stat}} \pm 0.08_{\text{sys}}$ where the photon flux is $\Phi \propto E^{-\Gamma}$). The LAT core spectrum, extrapolated to higher energies, is marginally consistent with the non-simultaneous HESS spectrum of the source. The LAT observations are complemented by simultaneous observations from *Suzaku*, the *Swift* Burst Alert Telescope and X-ray Telescope, and radio observations with the Tracking Active Galactic Nuclei with Austral Milliarcsecond Interferometry program, along with a variety of non-simultaneous archival data from a variety of instruments and wavelengths to produce a spectral energy distribution (SED). We fit this broadband data set with a single-zone synchrotron/synchrotron self-Compton model, which describes the radio through GeV emission well, but fails to account for the non-simultaneous higher energy TeV emission observed by HESS from 2004 to 2008. The fit requires a low Doppler factor, in contrast to BL Lac objects which generally require larger values to fit their broadband SEDs. This indicates that the γ -ray emission originates from a slower region than that from BL Lac objects, consistent with previous modeling results from Cen A. This slower region could be a slower moving layer around a fast spine, or a slower region farther out from the black hole in a decelerating flow. The fit parameters are also consistent with Cen A being able to accelerate ultra-high energy cosmic-rays, as hinted at by results from the Auger observatory.

Key words: galaxies: active – galaxies: individual (Centaurus A) – galaxies: jets – gamma rays: galaxies – radiation mechanisms: non-thermal

Online-only material: color figures

1. INTRODUCTION

Radio galaxies exhibiting jets which terminate in radio lobes on tens of kpc to Mpc scales are classified based on their radio

morphology and power by Fanaroff & Riley (1974). They are divided into Fanaroff–Riley (FR) type I and type II, where type I sources have the highest surface brightness feature at the center, while in type II sources it is farther from the core. Furthermore, the transition radio luminosity between FRI and FRII increases with the optical luminosity of the host galaxy (Ledlow & Owen 1996). In the active galactic nucleus (AGN) unification scheme, blazars are thought to be radio galaxies with

⁶⁸ Royal Swedish Academy of Sciences Research Fellow funded by a grant from the K. A. Wallenberg Foundation.

⁶⁹ Partially supported by the International Doctorate on Astroparticle Physics (IDAPP) program.

the jet aligned along our line of sight and are subdivided into flat spectrum radio quasars (FSRQs) and BL Lacertae objects based on the strength of emission lines in their spectrum, where FSRQs generally have strong emission lines, while BL Lac objects have weak emission lines or none at all (Strittmatter et al. 1972; Marcha et al. 1996; Landt et al. 2004). FRI galaxies are thought to correspond to misaligned BL Lac objects, while FRIIs correspond to misaligned FSRQs (e.g., Urry & Padovani 1995, and references therein), although there is evidence that this unification scheme is too simple (e.g., Landt & Bignall 2008). Apparent superluminal motion observed on milliarcsecond size scales indicates that their jets must be moving at high relativistic speeds, with bulk Lorentz factor $\Gamma_j \sim 10\text{--}20$ for FSRQs and BL Lac objects (Kellermann et al. 2004; Lister et al. 2009), although some TeV BL Lac objects have $\Gamma_j \sim 3$ (Piner et al. 2008). The existence of high energy and very high energy (VHE) γ -rays observed from these sources provides further evidence for highly relativistic flows, as they are necessary to avoid γ -ray attenuation by electron–positron pair production (Dondi & Ghisellini 1995). Indeed, this sometimes gives values of Γ_j greater than that found from very long baseline interferometry (VLBI) superluminal observations; e.g., $\Gamma_j \gtrsim 50$ is required for a recent outburst from PKS 2155–304 (e.g., Begelman et al. 2008; Finke et al. 2008).

Since blazars are strong sources of beamed γ -rays, it is natural to think that radio galaxies may also be. Several radio galaxies were detected by EGRET: 3C 111 (Hartman et al. 2008), NGC 6251 (Mukherjee et al. 2002), and Centaurus (Cen) A (Sreekumar et al. 1999; Hartman et al. 1999). The identifications were rather uncertain due to the large EGRET error circles. Only two radio galaxies have been definitively detected so far with the latest generation of TeV atmospheric Cherenkov telescopes, M87 (Aharonian et al. 2006; Acciari et al. 2008; Albert et al. 2008; Acciari et al. 2009a) and Centaurus A (Cen A; Aharonian et al. 2009). The radio galaxy 3C 66B seems to have been seen by MAGIC (Aliu et al. 2009), although the detection is questionable due to its proximity to the BL Lac object 3C 66A and its lack of detection by VERITAS (Acciari et al. 2009b). The *Fermi* Large Area Telescope (LAT) collaboration has reported the detections of NGC 1275 (Per A; Abdo et al. 2009b), M87 (Abdo et al. 2009d), and Cen A (Abdo et al. 2009c). Several more γ -ray detections of radio galaxies have been reported in the first *Fermi*-LAT catalog (1FGL; Abdo et al. 2010a, 2010b) and another publication will examine them in more detail (Abdo et al. 2010d).

The *Fermi* Gamma Ray Space Telescope was launched on 2008 June 11 and contains the LAT, a pair conversion telescope which has a field of view of about 20% of the sky at 20 MeV to over 300 GeV (Atwood et al. 2009). For the first year of operation, *Fermi* was operated in a sky-survey observing mode, wherein the LAT sees every point on the sky every ~ 3 hr.

During the first three months of science operation, the *Fermi*-LAT confirmed (Abdo et al. 2009a, 2009c) the EGRET detection of Cen A. Here with additional monitoring, we present accumulated data after 10 months of operation. The new LAT observations bridge the gap between EGRET and HESS, providing a detailed look at the γ -ray spectrum essential for addressing emission models. In addition to the LAT γ -ray source in the central few kpc (hereafter the γ -ray “core”), γ -rays from the giant lobes of Cen A have also been seen with *Fermi*, with the origin likely to be Compton scattering of the cosmic microwave background (CMB) and extragalactic background light (EBL), confirming the predictions of Cheung (2007) and

Hardcastle et al. (2009). Detailed work on separating the core and lobe emission is presented elsewhere (Abdo et al. 2010c, hereafter referred to as the lobe paper), although we provide a summary of LAT observations below. For the purposes of this paper, which is a study of γ -ray emission of the core, the lobes are essentially background sources.

We present a summary of Cen A and observations of this object in Section 2. The observations of the core of Cen A with the LAT over the first 10 months of *Fermi* operation are presented in Section 3. We also present simultaneous Cen A core observations from *Suzaku* and *Swift* and radio data from the Tracking Active Galactic Nuclei with Austral Milliarcsecond Interferometry (TANAMI) program in Section 4. In Section 5, we combine these with archival data and model its spectral energy distribution (SED) of the Cen A core. In Section 6 we discuss the implications in detail, and we conclude with a brief summary in Section 7.

2. CENTAURUS A

The FRI Cen A is the nearest radio-loud active galaxy to Earth, making it an excellent source for studying the physics of relativistic outflows and radio lobes. Indeed, it is near enough that its peculiar velocity dominates over the Hubble flow and its redshift ($z = 0.00183$) cannot be used to accurately calculate its distance. Ferrarese et al. (2007) have found that the average of several distance indicators gives $D = 3.7$ Mpc, which we adopt. At this distance, an arcsecond corresponds to about 18 pc. Due to its proximity to Earth, it has been well studied throughout the electromagnetic spectrum from radio to γ -rays. Recently, the Auger collaboration reported that the arrival directions of the highest energy cosmic rays ($\gtrsim 6 \times 10^{19}$ eV) observed by the Auger observatory are correlated with nearby AGN, including Cen A (Abraham et al. 2007, 2008), while Moskalenko et al. (2009) found that, if the giant lobes are taken into account, as many as four ultra-high energy cosmic rays (UHECRs) may be associated with this source. Although the overall significance of this correlation is reduced in the expanded Auger data set, the significance remains high in the direction of Cen A (Abraham et al. 2009). This suggests that Cen A—and other radio galaxies—may be sources of UHECRs.

Cen A has interesting radio structure on several size scales. The most prominent features are its giant radio lobes, which subtend $\sim 10^\circ$ on the sky, oriented primarily in the north–south direction. They have been imaged at 4.8 GHz by the Parkes telescope (Junkes et al. 1993) and studied at up to ~ 60 GHz by Hardcastle et al. (2009), utilizing *Wilkinson Microwave Anisotropy Probe* (WMAP; Hinshaw et al. 2009) observations. The north lobe contains a bright region a few tens of arcminutes in size often referred to as the northern middle lobe (Morganti et al. 1999). Misaligned by approximately 45° relative to the outer lobes are inner radio lobes on an arcminute scale (Burns et al. 1983). A strong, well-collimated jet can be seen on the arcsecond size scale in the radio, and *Chandra* can resolve X-ray emission from it, which is likely caused by synchrotron emission (Kraft et al. 2002; Hardcastle et al. 2003). The innermost region of Cen A has been resolved with VLBI and shown to have a size of $\sim 3 \times 10^{16}$ cm (Kellermann et al. 1997; Horiuchi et al. 2006). Observations at shorter wavelengths also reveal a small core, namely VLT infrared interferometry which resolves the core size to $\sim 6 \times 10^{17}$ cm (Meisenheimer et al. 2007). VLBI images reveal a weak counterjet on the milliarcsecond scale (Jones et al. 1996). Based on the motion of the VLBI blobs and assuming that the brightness differences of the different jets

are due to Doppler effects, Tingay et al. (1998) estimate the angle of the sub-parsec jet to our line of sight to be $\sim 50^\circ$ – 80° . Applying a similar technique to the 100 pc scale jet which has a larger jet-counterjet ratio, Hardcastle et al. (2003) estimate a jet angle of $\sim 15^\circ$. Hardcastle et al. (2003) speculate that the conflicting angle estimates may be due to the assumption that the jet-counterjet brightness differences are caused by Doppler beaming rather than intrinsic differences.

NGC 5128, the giant elliptical host galaxy of Cen A, contains a kiloparsec-scale dust lane. This feature appears to be an edge-on disk obscuring the central region and nucleus and is probably the remnant of a previous merger (Quillen et al. 1992; Israel 1998). It also has a dusty torus within 100 pc of the black hole, with a high column density ($N_H \gtrsim 10^{22} \text{ cm}^{-2}$; Israel et al. 2008; Weiß et al. 2008). X-ray spectra taken at various times over decade timescales indicate a time-varying absorbing column density, which could be due to variations in a warped disk viewed edge-on (Rothschild et al. 2006). Estimates for the mass of the supermassive black hole at the center of Cen A range $(0.5\text{--}1) \times 10^8 M_\odot$ (Silge et al. 2005; Marconi et al. 2006; Neumayer et al. 2007) based on the kinematics of stars, as well as H_2 and ionized gas.

With the *Compton Gamma-Ray Observatory*, emission was detected by OSSE (Kinzer et al. 1995) and COMPTEL (Steinle et al. 1998) at 100 s of keV–MeV energies. Kinzer et al. (1995) suggested the hard X-ray emission from Cen A detected with OSSE was the result of Compton-scattered disk radiation by a thermal plasma (i.e., a hot corona), due to a turnover in the spectra at a few hundred keV. However, Steinle et al. (1998) noted that the high-energy portions of the OSSE spectra are smoothly connected with the higher energy COMPTEL spectra and that the OSSE and COMPTEL variability seems to be correlated. They used this to argue for a nonthermal jet origin for the X-rays. Evans et al. (2004) have resolved the arcsecond-scale core of Cen A with *Chandra* and *XMM-Newton*. The 2–7 keV X-ray continuum, when corrected for absorption, is consistent with what is predicted from a correlation between unresolved X-ray emission and 5 GHz core emission for jets of radio galaxies (Canosa et al. 1999). They thus consider it likely that nonthermal emission from the sub-pc (sub-mas) scale jet is the origin of the continuum X-rays from the core of Cen A. However, hard X-rays observed by *Suzaku* do not seem to fit on the Canosa et al. (1999) correlation, possibly indicating a non-jet origin (Markowitz et al. 2007). The nature of the continuum X-ray emission from the core of Cen A remains an open question.

Cen A has been a target of γ -ray observations dating back to the 1970s (e.g., Grindlay et al. 1975; Hall et al. 1976). Cen A was seen by EGRET up to GeV energies (Sreekumar et al. 1999; Hartman et al. 1999). The γ -rays are thought to originate from a relativistic jet near the central elliptical galaxy (the radio “core”) analogous to blazars, although it has been suggested that Compton scattering of the CMB and the infrared-optical EBL in the giant radio lobes could be a source of γ -rays from Cen A (Hardcastle et al. 2009; Cheung 2007) and other radio galaxies such as Fornax A (Georganopoulos et al. 2008). At the highest TeV energies, a detection was recently reported from Cen A by the air Cherenkov detector HESS (Aharonian et al. 2009).

3. FERMI-LAT GAMMA-RAY OBSERVATIONS

3.1. Localization

The EGRET detection of Cen A (Sreekumar et al. 1999; Hartman et al. 1999) was confirmed early on by the

Fermi-LAT. Based on three months of all-sky survey data, the initial LAT detection was reported in the LAT bright source list (BSL) paper (Abdo et al. 2009a) as OFGL J1325.4–4303 with a 95% confidence localization, $r_{95} = 0^\circ:304 = 18'3$. In the companion LAT Bright AGN Sample paper (LBAS; Abdo et al. 2009c) to the BSL, a single power-law fit was reported, which gave $F(>100 \text{ MeV}) = 2.15 (\pm 0.45) \times 10^{-7} \text{ ph cm}^{-2} \text{ s}^{-1}$ with photon index, $\Gamma = 2.91 \pm 0.18$, and a peak flux on a ~ 1 week timescale of $(3.23 \pm 0.80) \times 10^{-7} \text{ ph cm}^{-2} \text{ s}^{-1}$. Note that this only considered the γ -ray emission from Cen A as a single point source, i.e., it did not account for any lobe emission.

To these initial observations, seven additional months of all-sky survey data are added to the current analysis. Specifically, the observations span the time period from 2008 August 4 to 2009 May 31, corresponding to mission elapsed time 239557420 – 265507200. Diffuse event class (CTBCLASSLEVEL = 3) events were selected with a zenith angle cut of $< 105^\circ$ and a rocking angle cut of 39° . The former are well calibrated and have minimal background while the latter greatly reduce Earth albedo γ -rays. For the analysis, LAT Science Tools⁷⁰ version v9r11 was utilized with the P6_V3_DIFFUSE instrument response function. The standard LAT Galactic emission model, GLL_IEM_V02.FIT⁷¹ was used, and the uniform background was represented by the isotropic diffuse γ -ray background and the instrumental residual background (isotropic_iem_v02.txt). We consider 11 point sources in the 1FGL catalog (Abdo et al. 2010a; see also Figure 1).

Figure 1 shows the 0.2–30 GeV LAT image centered on Cen A, which is clearly detected. Also prominent are the Galactic emission toward the south and several faint sources in the field. We obtained a localization of the source at Cen A with *gtfindsrc*, which finds point-source locations based on an unbinned likelihood analysis. The resulting localization was reduced to $r_{95} = 0^\circ:087 = 5'2$ (5.7 kpc), centered at R.A. = $201^\circ:399$, decl. = $-43^\circ:033$ (J2000.0 epoch) which is offset by $0^\circ:029 = 1'7$ (1.9 kpc) from the VLBI radio position of Cen A (Ma et al. 1998). Figure 2 shows the localization error circle of the LAT emission overlaid on the combined radio, optical, X-ray images. The new LAT position is consistent with that of 3EG J1324–4314 (Sreekumar et al. 1999; Hartman et al. 1999), but both are notably offset from EGR J1328–4337, the closest EGRET source in the Casandjian & Grenier (2008) catalog. The latter’s derived position shifted in such a way that Cen A was outside of the r_{95} localization circle, so that there was some ambiguity as to whether EGRET was actually detecting Cen A, but the new LAT position confirms the earlier 3EG result. The LAT significantly improves upon the previous EGRET γ -ray localization ($r_{95} = 0^\circ:53 = 32'$).

3.2. Spatial and Spectral Analysis

The binned likelihood fitting was performed with the *gtlike* tool, first assuming that Cen A is a point source, i.e., that there is no γ -ray lobe emission (model A). The field point-source positions were fixed, and their spectra were assumed to be power laws, with the photon indices allowed to vary. The location of Cen A was fixed at its VLBI radio position (Ma et al. 1998). In addition to the 11 1FGL point sources used in the lobe paper, in order to treat the lobe emission as a background source, we include two 1FGL sources, 1FGL J1322.0–4515 and 1FGL J1333.4–4036, which are thought to be the local maxima of the

⁷⁰ <http://fermi.gsfc.nasa.gov/ssc/data/analysis/scitools/overview.html>

⁷¹ <http://fermi.gsfc.nasa.gov/ssc/data/access/lat/BackgroundModels.html>

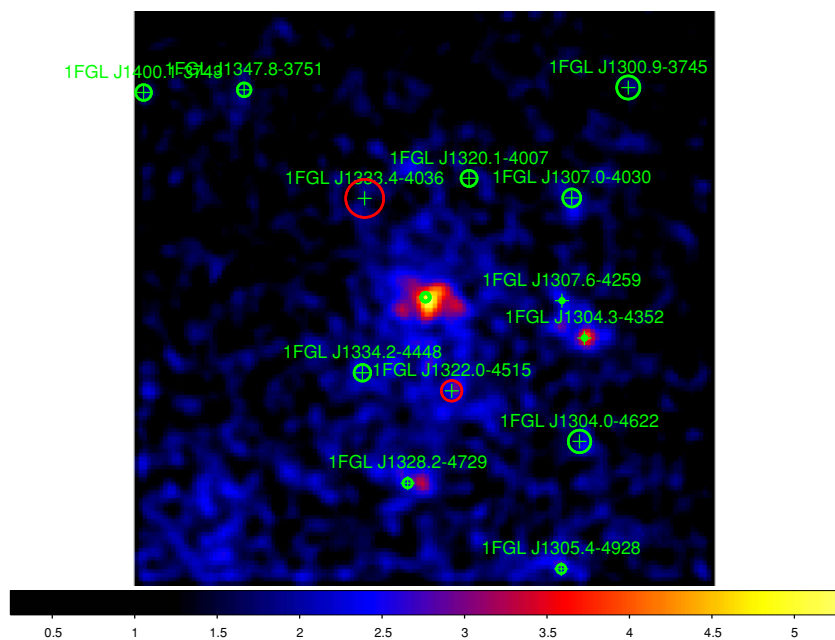


Figure 1. LAT gamma-ray image in the 0.2–30 GeV range in a $14^\circ \times 14^\circ$ region, smoothed by a Gaussian with $\sigma = 0.3$. The green crosses are the source in the 11-month LAT source list. Green circles are sources considered in the likelihood fitting for model B (see the lobe paper). Red circles are additional sources considered in the 11-month catalog.

(A color version of this figure is available in the online journal.)

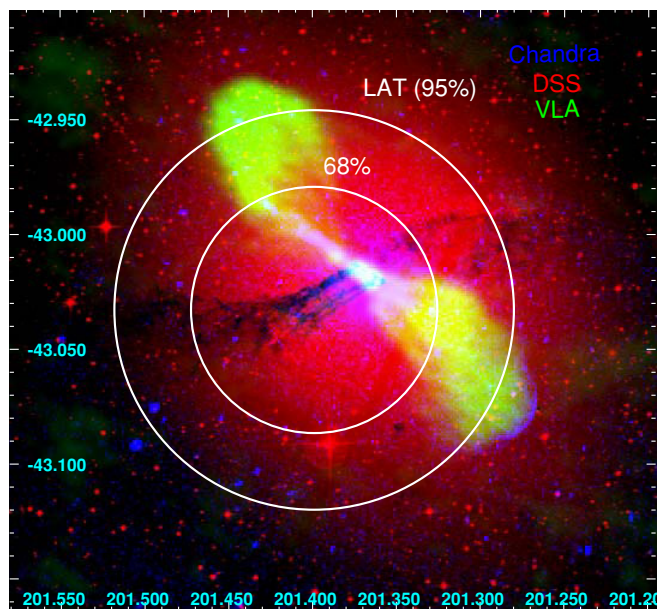


Figure 2. LAT localization error circles indicated on a three-color image of Cen A. The image is made with the VLA 21 cm image from Condon et al. (1996), the optical from Digital Sky Survey plates from the UK 48 inch Schmidt telescope, and an archival *Chandra* X-ray exposure from (Hardcastle et al. 2007, OBSID 7797). The γ -ray source is clearly positionally coincident with Cen A, enclosing the core, kpc-scale jet, and most of the radio lobes.

(A color version of this figure is available in the online journal.)

lobe emission. A likelihood analysis with the energy information is binned logarithmically in 20 bins in the 0.2–30 GeV band, and the γ -ray directions binned into a $14^\circ \times 14^\circ$ grid with a bin size of 0.1×0.1 . For both the Galactic and isotropic emission models, one free parameter was introduced to adjust the normalization. Because the effective area of the LAT is rapidly changing below ~ 200 MeV, we use events with energy above this value. Above

30 GeV the significance of detection is $< 3\sigma$, so we make a cut as this energy as well.

As a result, the test statistic (TS; Mattox et al. 1996) is found to be 378 for Cen A, which is smaller than the $TS = 628$ in the 1FGL catalog (Abdo et al. 2010a), since the lower energy limit is 200 MeV in our analysis instead of 100 MeV in the catalog. The relative normalizations of the Galactic and isotropic models become 1.02 ± 0.02 and 1.40 ± 0.06 , respectively, and the fit is reasonable within the current background model uncertainty. This fit gives a power-law photon index of Cen A between 200 MeV and 30 GeV of $\Gamma = 2.76 \pm 0.07$ and the flux extrapolated down to > 100 MeV is $(2.06 \pm 0.20) \times 10^{-7}$ ph cm $^{-2}$ s $^{-1}$ (where errors are statistical only). As noted in Abdo et al. (2009c), the spectrum is very steep in comparison to the typical blazars of $\Gamma = 1.5$ – 2.5 . The power-law photon index is consistent with the 3EG result of $\Gamma = 2.58 \pm 0.26$ (Hartman et al. 1999). The 3EG flux was reported to be $(1.36 \pm 0.25) \times 10^{-7}$ ph cm $^{-2}$ s $^{-1}$ with a peak value of $(3.94 \pm 1.45) \times 10^{-7}$ ph cm $^{-2}$ s $^{-1}$ (Hartman et al. 1999), consistent with the average flux.

We next modeled the region with a radio image of the giant lobe (model B). This analysis is identical to that described in the lobe paper, and the reader is referred to it for details. We present a brief description below. We use the *WMAP* image at 20 GHz from Hardcastle et al. (2009) and eliminate the Cen A core region with a cut radius of 1° . In this analysis, we exclude two point sources (1FGL J1322.0–4515 and 1FGL J1333.4–4036), which are assumed to be emission from the lobes. The binned likelihood analysis was performed to extract the flux and spectral indices for the core and lobes. The relative normalizations of the Galactic and isotropic models become 1.00 ± 0.02 and 1.44 ± 0.06 , respectively. The γ -ray detection in each energy range is significant at a 4σ level up to the 5.6–10 GeV energy bin for the core region, and the spectrum is consistent with the power-law model. This fit gives a photon index of the core between 200 MeV and 30 GeV of $\Gamma = 2.67 \pm 0.10_{\text{stat}} \pm 0.08_{\text{sys}}$ and a flux

Table 1
Summary of Multiwavelength Observations

Instrument	Observation Date	Exposure Time	Frequency/Energy Range
Australian LBA and IVS	2009 November 27	3.6 ks	22.3 GHz
	2009 November 29	3.6 ks	8.4 GHz
<i>Suzaku</i> XIS	2009 July 20–August 16	150 ks	0.4–10 keV
<i>Suzaku</i> HXD	2009 July 20–August 16	150 ks	10–300 keV
<i>Swift</i> XRT	2009 January 15–28	22 ks	0.2–10 keV
<i>Swift</i> BAT	2008 August–2009 May	1.9 Ms	14–200 keV
<i>Fermi</i> LAT	2008 August 4–2009 May 31	10 months	0.2–30 GeV

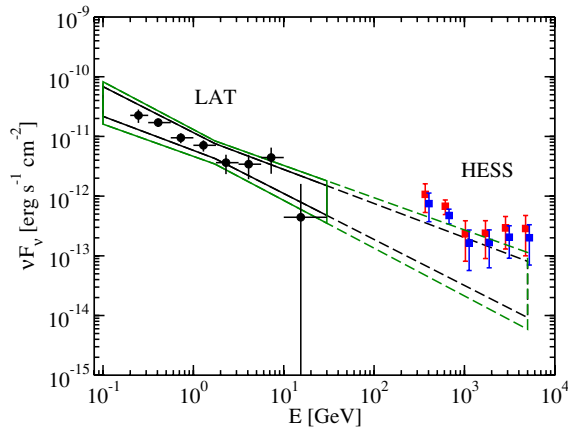


Figure 3. Spectrum of the Cen A core from differential fluxes derived for successive energy ranges from model B (black circles). The black bowtie indicates the best-fit 0.1–30 GeV LAT flux and Γ with statistical errors only, while the green bowtie indicates this with systematic errors as well. The LAT spectrum is extrapolated into the HESS energy range (dashed lines). The HESS data from Aharonian et al. (2009) are shown (red squares) and the HESS data shifted to lower flux by their statistical and systematic normalization error (blue squares). The latter are also shifted in energy by 10% for clarity.

(A color version of this figure is available in the online journal.)

extrapolated down to >100 MeV of $(1.50 \pm 0.25_{\text{stat}} \pm 0.37_{\text{sys}}) \times 10^{-7}$ ph cm $^{-2}$ s $^{-1}$, with statistical and systematic errors reported. Here, we consider the systematic errors from the effective area, the diffuse model, and *WMAP* inner cut radius, as described in the lobe paper. The photon index is almost identical to that of model A, but the flux is somewhat lower due to some of the core photons from model A being considered as being emitted by the lobes in model B. The results for model B can be seen in Figure 3.

3.3. Time Variability

To quantify variability within the ~ 10 months of LAT observation, we generated light curves in 30 and 15 day bins using the binned likelihood analysis with *gtlike*. We performed the analysis taking into account the lobe emission (i.e., model B in Section 3.2). The power-law normalizations of the core and background point sources are treated as free parameters, but the photon indices of all sources and the normalizations of the lobes and the diffuse background models are fixed to the values obtained in the 200 MeV–30.0 GeV range for the whole time region. Figure 4(a) shows the light curve of the flux (extrapolated down to >100 MeV) in 30 day bins. The χ^2 test results in $\chi^2/\text{dof} = 0.98$, and the light curve with 15 day bins gives $\chi^2/\text{dof} = 0.89$. These are consistent with no variability. The time behavior of Cen A is in contrast to large variability of typical blazars in the MeV/GeV range and similar to that of Perseus A (Abdo et al. 2009b) and M87 (Abdo et al. 2009d).

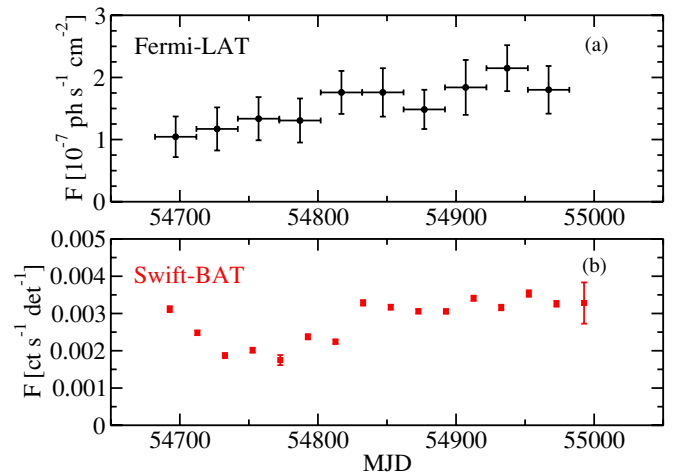


Figure 4. (a) *Fermi*-LAT light curve of Cen A without considering lobe emission (model A) in 30 day bins, and (b) simultaneous light curve from *Swift*-BAT (14 day bins).

(A color version of this figure is available in the online journal.)

4. OTHER CONTEMPORANEOUS OBSERVATIONS

Observations with several different instruments, both on the Earth and in space, were made during the 10 months of LAT observations presented here. Cen A was observed in the radio as part of the TANAMI program (Mueller et al. 2009; Ojha et al. 2009). Data were taken with two instruments on the *Swift* spacecraft (Gehrels et al. 2004) and two instruments on the *Suzaku* spacecraft (Mitsuda et al. 2007; Koyama et al. 2007; Takahashi et al. 2007). A summary of these observations can be found in Table 1, and descriptions are given below.

4.1. Southern Hemisphere LBA Observations

Cen A was observed with VLBI on 2009 November 27/29, as part of the TANAMI program using the five antennas of the Australian Long Baseline Array (LBA), the 70 m DSS-43 antenna at NASA's Deep Space Network at Tidbinbilla, Australia, and two trans-oceanic telescopes TIGO (Chile) and O'Higgins (Antarctica) of the International VLBI Service (IVS) for Geodesy and Astrometry (the latter two participating at 8.4 GHz, only). The beam size achieved was $(0.92 \text{ mas} \times 0.56 \text{ mas})$ at 8.4 GHz and $(1.68 \text{ mas} \times 1.25 \text{ mas})$ at 22.3 GHz using natural weighting. These observations were part of the TANAMI monitoring of a radio and γ -ray selected sample of 65 blazars at 8.4 GHz and 22.3 GHz with observations approximately every two months.

TANAMI data are correlated on the DiFX software correlator (Deller et al. 2007) at Curtin University in Perth, Western Australia. Data inspection and fringe fitting was done with

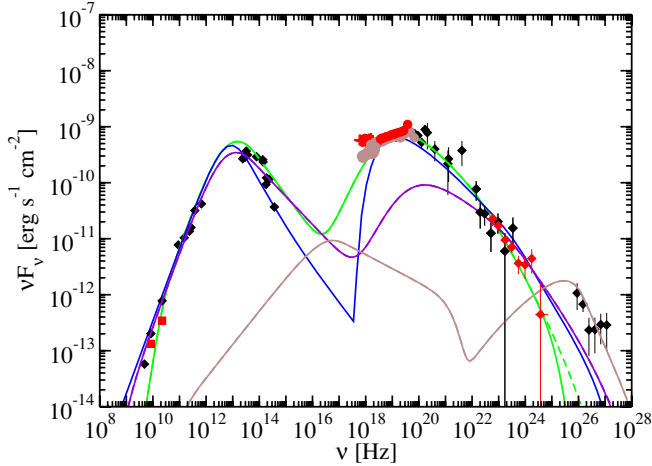


Figure 5. SED of the Cen A core with model fits. Colored symbols are observations between 2009 August and May, the epoch of the LAT observations. These include observations from low to high frequency: the TANAMI VLBI (red squares), *Swift*-XRT (red crosses), *Suzaku* (brown circles), *Swift*-BAT (red circles), and *Fermi*-LAT (red diamonds). Black symbols are archival data (Marconi et al. 2000), including HESS observations (Aharonian et al. 2009). Curves are model fits to nuclear region of Cen A. The green curve is a synchrotron/SSC fit to the entire data set. The dashed green curve shows this model without $\gamma\gamma$ attenuation. The violet curve is a similar fit but is designed to under fit the X-ray data, and the brown curve is designed to fit the HESS data while not overproducing the other data in the SED. The blue curve is the decelerating jet model fit (Georganopoulos & Kazanas 2003). See Table 2 for the parameters of these model curves.

(A color version of this figure is available in the online journal.)

AIPS (National Radio Astronomy Observatory’s Astronomical Image Processing System software). The images were produced by applying the program DIFMAP (Shepherd 1997), using the CLEAN algorithm. More details about the data reduction can be found in Ojha et al. (2005).

Data from the first epoch (November 2009) of TANAMI observations are presented in Ojha et al. (2009). Figure 5 includes the fluxes at 22.3 GHz and 8.4 GHz measured on 2009 November 27 and 29, respectively. The total flux density, corresponding to the emission distributed over the inner ~ 120 mas at 8.4 GHz, is $S_{\text{total}} = 3.90$ Jy. At 22.3 GHz, a total VLBI flux density of 3.2 Jy is distributed over the inner ~ 40 mas of the jet, with very little emission on the counterjet side.

Via model fitting, we found a component with an inverted spectrum, which is the brightest at both frequencies and which we identify with the jet core. The core flux density is 0.92 Jy at 8.4 GHz and 1.54 Jy at 22.3 GHz. The core size is consistently modeled at both frequencies to be $(0.9\text{--}1.0)$ mas \times $(0.29\text{--}0.31)$ mas at the same position angle of $53^\circ\text{--}55^\circ$ (see Ojha et al. 2009).

4.2. *Suzaku* Observations

Cen A was observed with *Suzaku* on 2009 July 20–21, August 5–6, and August 14–16 with a total exposure of 150 ks, during which time the flux approximately doubled. We utilized data processed with version 2.4 of the pipeline *Suzaku* software and performed the standard data reduction: a pointing difference of $<1'$, an elevation angle of $>5^\circ$ from the Earth rim, and a geomagnetic cut-off rigidity (COR) of >6 GV. We did not use events from the time the spacecraft entered the South Atlantic Anomaly (SAA) to 256 s after it left the SAA. Further selection was applied: Earth elevation angle of $>20^\circ$ for the X-ray Imaging Spectrometer (XIS), COR > 8 GV, and the time elapsed

from the SAA (T_SAA_HXD) of >500 s for the Hard X-ray Detector (HXD). The XIS response matrices are created with *xismfgen* and *xissimarfgen* (Ishisaki et al. 2007). The HXD responses used here are *ae_hxd_pinhxnome5_20070914.rsp* for the PIN and *ae_hxd_gsohxnom_20060321.rsp* and *ae_hxd_gsohxnom_20070424.arf* for the Gadolinium Silicate (GSO) crystal. The “tuned” (LCFIT) HXD background files (Fukazawa et al. 2009) are utilized. The detailed *Suzaku* analysis, including time variability, will be reported elsewhere (Y. Fukazawa et al. 2010, in preparation). The *Suzaku* data were fit with a single absorbed power law, which was found to have a spectral index $\Gamma = 1.66 \pm 0.01$ with dust-absorbing column density $N_H = (1.08 \pm 0.01) \times 10^{23} \text{ cm}^{-2}$. The flux in the 12–76 keV band in 2009 July was $(1.23 \pm 0.01) \times 10^{-9} \text{ ergs}^{-1} \text{ cm}^{-2} \text{ keV}^{-1}$, about twice the flux measured by *Suzaku* in 2005 (Markowitz et al. 2007).

4.3. *Swift*-XRT Observations

Cen A was observed on six days between 2009 January 15 and 28 for a total exposure of 22 ks (see Table 1). The XRT (Burrows et al. 2005) data were processed with the XRTDAS software package (v. 2.5.1) developed at the ASI Science Data Center and distributed by the NASA High Energy Astrophysics Archive Research Center within the HEASoft package (v. 6.6). Event files were calibrated and cleaned with standard filtering criteria with the *xrtpipeline* task using the latest calibration files available in the *Swift* CALDB.

The XRT data set was taken entirely in Windowed Timing mode. For the spectral analysis, we selected events in the energy range 2–10 keV with grades 0–2. The source events were extracted within a box of 40×40 pixels (~ 94 arcsec), centered on the source position and merged to obtain the average spectrum of Cen A during the XRT campaign. The background was estimated by selecting events in a region free of sources. Ancillary response files were generated with the *xrtmkarf* task applying corrections for the point-spread function losses and CCD defects.

The combined January X-ray spectrum is highly absorbed. Hence, it was fitted with an absorbed power-law model with a photon spectral index of 1.98 ± 0.05 , an intrinsic absorption column of $(9.73 \pm 0.26) \times 10^{22} \text{ cm}^{-2}$, in excess of the Galactic value of $8.1 \times 10^{20} \text{ cm}^{-2}$ in that direction (Kalberla et al. 2005). The average absorbed flux over the 2–10 keV energy range is $(4.94 \pm 0.05) \times 10^{-10} \text{ erg cm}^{-2} \text{ s}^{-1}$, which corresponds to an unabsorbed flux of $9.15 \times 10^{-10} \text{ erg cm}^{-2} \text{ s}^{-1}$.

The XRT spectrum included in the broadband SED was binned to ensure a minimum of 2500 counts per bin and was de-absorbed by forcing the absorption column density to zero in XSPEC and applying a correction factor to the original spectrum equal to the ratio of the de-absorbed spectral model over the absorbed model.

4.4. *Swift*-BAT Observations

We used data from the Burst Alert Telescope (BAT) on board the *Swift* mission to derive a 14–195 keV spectrum of Cen-A contemporary to the LAT observations. The spectrum has been extracted following the recipes presented in Ajello et al. (2008, 2009b). This spectrum is constructed by calculating weighted averages of the source spectra extracted over short exposures (e.g., 300 s). These spectra are accurate to the mCrab level and the reader is referred to Ajello et al. (2009a) for more details.

5. SED AND MODELING

5.1. Spectral Energy Distribution

The LAT spectrum of the core of Cen A is shown in Figure 3, extrapolated into the TeV regime, along with the HESS spectrum observed between 2004 and 2008 (Aharonian et al. 2009). Also shown is the HESS spectrum scaled down by its source flux normalization uncertainty. It seems that the LAT spectrum, with its statistical and systematic errors and extrapolated to higher energies, is just barely consistent with the HESS spectrum. However, one should keep in mind that the HESS and LAT spectra presented in this figure are not simultaneous, although the HESS data did not show any signs of variability. Additionally, $\gamma\gamma$ absorption makes it unlikely that the HESS and LAT emission originate from the same region, which is explored below (Section 5.2).

Since the cores of many blazars have been shown to be γ -ray loud, it is plausible to assume that the radio core is the source of the central γ -rays from Cen A. However, one should keep in mind that the error circles of the *Fermi* and HESS (Aharonian et al. 2009) observations are consistent with emission from the inner lobes, jet and radio core, so that these other regions could be sources of γ -rays as well. We construct the SED for the resolved sub-arcsec and arcsec-scale core as compiled in Meisenheimer et al. (2007), including their mm/IR/optical observations from 2003 to 2005. They have compiled additional points from the 1990s and have applied an extinction correction of $A_V = 9$ mag to the optical and IR data. We plot historical data in the X-ray (Evans et al. 2004), hard X-rays (Kinzer et al. 1995; Rothschild et al. 2006; Markowitz et al. 2007), COMPTEL (Steinle et al. 1998), and the HESS TeV γ -rays (Aharonian et al. 2009). The *Swift* XRT and BAT as well as *Suzaku* data, corrected for Galactic dust as well as dust in NGC 5128 and discussed in Section 4, were collected during time intervals which overlap with much of the *Fermi*-LAT data. Furthermore, we add the simultaneous radio data of the TANAMI VLBI jet components. All these are shown in Figure 5. The LAT data points in Figure 5 are from model B and include statistical errors only.

5.2. Synchrotron/Synchrotron self-Compton Model

Single-zone synchrotron/synchrotron self-Compton (SSC) models have been very successful in explaining the multi-wavelength (including γ -ray) emission from BL Lac objects (e.g., Bloom & Marscher 1996; Tavecchio et al. 1998). If FRIs are the misaligned counterpart to BL Lac objects, one would expect this model to apply to them as well. In the synchrotron/SSC scenario the low energy, radio through optical emission originates from nonthermal synchrotron radiation from a relativistically moving spherical homogeneous plasma blob, and the X-ray through VHE γ -rays from the Compton scattering of that synchrotron radiation by electrons in the same blob. The one-zone SSC model has successfully fit the emission from the other *Fermi*-LAT detected FRIs, Perseus A (NGC 1275; Abdo et al. 2009b) and M87 (Abdo et al. 2009d), and has been successfully applied to previous observations of Cen A (Chiaberge et al. 2001). Here, we apply the single-zone SSC model to fit the recent multiwavelength observations of Cen A, particularly the *Fermi*-LAT and HESS emission.

One can show (see the Appendix) that, on the assumption that all of the emission in the multiwavelength SED of the Cen A core originates from the same region in a single-zone SSC model,

$\gamma\gamma$ absorption gives the constraint on the Doppler factor

$$\delta_D \geq 5.3 \quad (1)$$

where the Doppler factor is $\delta_D = [\Gamma_j(1 - \beta_j\mu)]^{-1}$, the bulk Lorentz factor of the jet is $\Gamma_j = (1 - \beta_j^2)^{-1/2}$, $\beta_j c$ is the speed of the jet, and $\theta = \cos^{-1} \mu$ is the angle of the jet with respect to our line of sight. Solving for Γ_j in terms of δ_D ,

$$\Gamma_j = \frac{1 \pm \sqrt{1 - (1 - \mu^2)(1 + \delta_D^2 \mu^2)}}{\delta_D(1 - \mu^2)}. \quad (2)$$

In order for Γ_j to be real, the quantity under the radical must be positive, which implies

$$\delta_D \leq \frac{1}{\sqrt{1 - \mu^2}} = \csc \theta \quad (3)$$

(e.g., Urry & Padovani 1995). For Cen A, estimates of θ vary from 15° to 80° (see Section 2). For the least constraining value, i.e., $\theta = 15^\circ$,

$$\delta_D \leq 3.8. \quad (4)$$

Clearly, the constraints (1) and (4) are not compatible. Thus, if the radio through *Fermi* γ -ray data presented in Figure 5 is synchrotron and SSC emission originating from the same region of the jet, then *the HESS emission cannot originate from the same part of the jet*. Note also that the HESS emission cannot originate from the same region of the jet, yet be emitted from a different mechanism from SSC (say, Compton-scattered accretion disk or dust torus radiation) because even this radiation would be subject to the same $\gamma\gamma$ attenuation by synchrotron photons.

If the VLBI jet core is assumed to be the origin of the high-energy emission, the TANAMI core-size measurement can be used to calculate an upper limit on the size of the γ -ray emitting region of <0.017 pc = 5.3×10^{16} cm (Section 3.1). This is consistent with the VLBI observations of Kellermann et al. (1997) and Horiuchi et al. (2006) and with a variability timescale of $t_v \sim 1$ day, given that the emitting region radius R_b is constrained by the variability time by $R_b = \delta_D c t_v$. This variability timescale is consistent with the *Suzaku* observations, although it is not clear that the *Suzaku* X-rays come from the same region as the γ -rays. Using this variability timescale and Equations (A1) and (A2), one gets $\delta_D = 0.6$ and $B = 6$ G. More precise modeling (Finke et al. 2008) gives the green curve in Figure 5 with the model parameters in Table 2. This curve demonstrates that the emission can be fit with a Doppler factor of unity. This is consistent with a Lorentz factor of unity or 7, a degeneracy which can be seen in Equation (2). A stationary, nonrelativistic jet can explain the entire SED, except the VHE emission. This fit is similar to the synchrotron/SSC fit by Meisenheimer et al. (2007) who fit similar data. We further note that a small change in δ_D leads to a large change in the Lorentz factor. This, combined with the uncertainty in the inclination angle leads to the fact that the Lorentz factor is not well constrained by modeling. We also note that VLBI observations show *apparent* motion with $\beta_{j,\text{app}} \sim 0.1$ (Tingay et al. 1998), implying $\Gamma_j \gtrsim 1.005$, which is also not a particularly strong constraint.

What if the hard X-ray emission originates from thermal Comptonization near the disk, and not from jet emission? If we assume that the rest of the high-energy SED is from the jet,

Table 2
Model Parameters

Parameter	Symbol	Green ¹	Blue ²	Violet ³	Brown ⁴
Bulk Lorentz factor	Γ_j	7.0	5 \rightarrow 2	3.7	2.0
Doppler factor	δ_D	1.0	1.79 \rightarrow 1.08	3.9	3.1
Jet angle	θ	30°	25°	15°	15°
Magnetic field (G)	B	6.2	0.45	0.2	0.02
Variability timescale (s)	t_v	1.0×10^5		1×10^5	1×10^5
Comoving blob size scale (cm)	R_b	3.0×10^{15}	3×10^{15}	1.1×10^{16}	9.2×10^{15}
Low-energy electron spectral index	p_1	1.8	3.2	1.8	1.8
High-energy electron spectral index	p_2	4.3		4.0	3.5
Minimum electron Lorentz factor	γ_{\min}	3×10^2	1.3×10^3	8×10^2	8×10^2
Maximum electron Lorentz factor	γ_{\max}	1×10^8	1×10^7	1×10^8	1×10^8
Break electron Lorentz factor	γ_{brk}	8×10^2		2×10^3	4×10^5
Jet power in magnetic field (erg s ⁻¹)	$P_{j,B}$	6.5×10^{43}	1.7×10^{41}	2.7×10^{41}	4.3×10^{38}
Jet power in electrons (erg s ⁻¹)	$P_{j,e}$	3.1×10^{43}	3.1×10^{42}	2.3×10^{42}	7.0×10^{40}

¹ SSC model.

² Decelerating Jet model (Georganopoulos & Kazanas 2003).

³ SSC model excluding X-rays.

⁴ SSC Fit to HESS data only.

then $\epsilon_{\text{pk}}^{\text{SSC}} = 1$ and $f_{\text{pk}}^{\text{SSC}} = 9 \times 10^{-11} \text{ erg s}^{-1} \text{ cm}^{-2}$, so that Equations (A1) and (A2) give $\delta_D = 2.4$ and $B = 0.6 \text{ G}$ for a variability timescale of 1 day. More detailed modeling gives the violet curve seen in Figure 5 with the parameters in Table 2. The larger Doppler factor needed for this model requires a smaller angle to the line of sight. The Lorentz factor is again not strongly constrained and could plausibly be as high as $\Gamma_j \sim 8$ and still provide a good fit, although this would push the parameters to their extremes. This model still underpredicts the HESS data.

Jet powers for these models are given in Table 2. The proton and pair content of the jet are not well known, so the total jet power presented in Table 2 is for a pure pair jet and can be considered a lower limit. Even with 10–100 times more energy in ions than leptons, the absolute jet power is far below the Eddington luminosity for a $10^8 M_\odot$ black hole ($L_{\text{Edd}} = 1.3 \times 10^{46} \text{ erg s}^{-1}$). For the green curve, the parameters assume $\Gamma = 7$. The jet power needed to inflate the giant lobes of Cen A in their lifetime, as inferred from the radio spectral break, is $10^{43} \text{ erg s}^{-1}$ (Hardcastle et al. 2009). This value is approximately consistent with the green curve model presented in Figure 5.

A possible explanation for the HESS observations is that the TeV emission is produced by another blob. We show in Figure 5 (brown curve) that another synchrotron/SSC-emitting blob can produce the HESS emission without overproducing any of the other multiwavelength data. The parameters for this blob are given in Table 2, although this fit is not unique and many parameter sets would fit the HESS data and not contribute at other wavelengths. Other possible origins for the VHE emission are discussed in Section 6.1.

5.3. Decelerating Jet Model

Unification models for blazars suggest that FR II galaxies are FSRQs with the jet viewed away from our line of sight, and similarly FR I are the parent population of BL Lac objects. In this case, one would expect nonthermal emission from the cores of radio galaxies de-beamed compared to blazars. However, the cores of FR I seem brighter than what is expected from simply de-beamed emission from BL Lac objects, which implies that the radio galaxy core emission is from a slower region than that of BL Lac objects, since the beaming angle is related to the bulk

Lorentz factor by $\theta_b \sim 1/\Gamma_j$. There are (at least) two possible explanations for this: (1) the jet consists of a faster “spine,” which is responsible for the on-axis blazar emission, inside a slower outer “sheath,” which would be responsible for the off-axis emission seen in the cores of radio galaxies (e.g., Chiaberge et al. 2000); and (2) a decelerating jet model where the on-axis blazar emission is produced by a faster flow closer to the black hole and the off-axis γ -rays seen in radio galaxies are produced by the slower flow farther out along the jet (Georganopoulos & Kazanas 2003).

As an example, we provide a fit to the Cen A SED using this decelerating flow, as the blue curve in Figure 5. In this model, the high-energy emission is due to upstream Compton scattering of synchrotron photons produced in the slower part of the flow being scattered by energetic electrons in the faster, upstream part of the flow. The jet starts with a bulk Lorentz factor $\Gamma_{j,\text{max}} = 5$ and decelerates down to $\Gamma_{j,\text{min}} = 2$ in a length of $l = 3 \times 10^{16} \text{ cm}$. The injected power-law electron distribution, $n(\gamma) \propto \gamma^{-p}$, has an index $p = 3.5$ and extends from $\gamma_{\min} = 1600$ to $\gamma_{\max} = 10^7$, and the magnetic field at the inlet is $B = 0.3 \text{ G}$. Jet powers for this model are similar to the one-zone SSC model fits presented in Section 5.2, although this decelerating model fit is particle dominated rather than magnetic field-dominated. We also note that the parameters used in this fit are not unique.

6. DISCUSSION

6.1. Origin of VHE γ -ray Emission

Since the single blob model does not seem to be able to reproduce the broadband SED of Cen A, could something else be the origin of the VHE γ -rays? We have already shown that another blob emitting synchrotron and SSC radiation could explain the HESS emission without overproducing any of the other data (Figure 5, brown curve). Lenain et al. (2008) have presented a model with multiple blobs, moving at different angles to the line of sight from a large opening angle, to M87 and Cen A (among other objects). This model does seem to be able to explain this SED (Lenain et al. 2009). It has also been suggested that absorbed γ -rays create e^+e^- pairs, creating an isotropic halo of electrons in the interstellar medium which

Compton-scatter the host galaxy’s starlight, and lead to isotropically produced γ -rays (Stawarz et al. 2003, 2006). The HESS data do seem to match the Stawarz et al. (2006) predictions Cen A with a galactic magnetic field of 10 μ G. Compton-scattering off of leptons accelerated by the supermassive black hole magnetosphere, similar to particle acceleration in pulsars, has been proposed to explain the VHE γ -ray radiation from M87 (Neronov & Aharonian 2007). This could also explain the HESS data from Cen A separate from the other multiwavelength emission. As we have noted earlier, what we designate in this paper as the γ -ray “core” actually encompasses the radio core, jet, and inner lobes of Cen A. This is also true for the HESS emission. Croston et al. (2009) have noted that a shock front observed in X-rays in the southwest inner lobe could be a source of TeV γ -rays, which seems consistent with these observations.

Finally, we note that the SED presented here is constructed from non-simultaneous data. Although *Fermi* and HESS γ -rays do not show appreciable variability, they could still be variable on longer timescales. Perhaps for a good, simultaneous multiwavelength SED, a one-zone synchrotron/SSC model could provide a good fit to all of the data. Probably the best way to discriminate between the above models—simple SSC, Compton-scattering emission from a pair halo, multiple blobs, etc.—is correlated variability between LAT γ -rays and other bandpasses. This emphasizes the importance of simultaneous multiwavelength data.

6.2. Origin of UHE Cosmic Rays

The Auger Observatory results indicate that some UHECRs could be originating from Cen A (see Section 2). The UHECRs could interact with photons at the source and in the extragalactic background light leading to an observable signature in the HESS band. If the VHE γ -rays originate from cosmic rays, this could account for the discrepancy between HESS and *Fermi* γ -rays. Based on the green curve fit presented in Figure 5, we can analyze whether it is plausible for cosmic rays to originate from Cen A, keeping in mind that the parameters of that model are not well constrained (Section 5.2).

The maximum energy to which cosmic rays can be accelerated is limited by the size scale of the emitting region and the highest energy they can reach before they are cooled. The former constraint implies that the highest energy a cosmic ray can reach is

$$E_Z = 4 \times 10^{19} \frac{Z}{\phi} \left(\frac{B}{6.2 G} \right) \left(\frac{t_v}{10^5 s} \right) \delta_D \left(\frac{\Gamma_j}{7.0} \right) \text{ eV}, \quad (5)$$

and the latter implies

$$E_Z = 5.7 \times 10^{20} \sqrt{\frac{Z}{\phi}} \left(\frac{A}{Z} \right)^2 \left(\frac{B}{6.2 G} \right)^{-1/2} \left(\frac{\Gamma_j}{7.0} \right) \text{ eV} \quad (6)$$

(e.g., Hillas 1984; Dermer & Razzaque 2010), where $\phi \approx 1$ is the acceleration efficiency factor, e is the elementary charge, Z is the atomic number, and A the atomic mass of the ion. Note that these timescales, and all quantities expressed above, are in the frame comoving with the blob, although for the particular model considered here $\delta_D = 1$; so this is not important.

We assume that all parameters have values from the green curve model. Thus, it seems for this model that it is unlikely that protons will be accelerated to energies above $\approx 4 \times 10^{19}$ eV, although it is possible for heavier ions to be accelerated this high before they are disintegrated by interacting with

infrared photons from the Cen A core. The threshold energy for photomeson interaction with peak synchrotron photons is similar to E_Z . This process could create observational signatures from secondary emission (e.g., Kachelrieß et al. 2009), as well as convert protons to neutrons, which can escape as cosmic rays (Dermer et al. 2009). Again, we note that this result is strongly model-dependent, and the parameters of this model are not strongly constrained, so this limit should not be taken too seriously. For example, a small change in the Doppler factor would have little effect on the model fit but would require a large change in the bulk Lorentz factor, Γ_j . A large change in Γ_j would significantly affect the highest energy to which particles could be accelerated, as seen in Equations (5) and (6). Furthermore, if we are viewing a slower sheath, UHE cosmic rays could be accelerated in the faster spine beamed away from our line of sight, which could have significantly different parameters. Acceleration of protons up to 10^{20} eV requires jet powers of $P_j \gtrsim 10^{46}$ erg s^{-1} , which may take place in occasional flaring activities in Cen A (Dermer et al. 2009).

7. SUMMARY

We have reported on observations of Cen A with the LAT instrument on board the *Fermi Gamma-Ray Space Telescope*. This instrument’s excellent angular resolution compared to other γ -ray detectors at MeV–GeV energies makes it possible for the first time to separate the lobe and core emission. The LAT observations have been supplemented with simultaneous observations from *Suzaku*, *Swift*, the Australia Telescope Long Baseline Array, and a variety of non-simultaneous data, including those from HESS. Our results are as follows.

1. The LAT-detected core position is consistent with Cen A’s VLBI core (Ma et al. 1998) and previous EGRET observations (Hartman et al. 1999).
2. With 10 months of LAT exposure, we find the core flux >100 MeV to be $(1.50 \pm 0.25_{\text{stat}} \pm 0.37_{\text{sys}}) \times 10^{-7}$ ph $\text{cm}^{-2} \text{s}^{-1}$ and the spectral index in the 0.2–30 GeV range to be $\Gamma = 2.67 \pm 0.10_{\text{stat}} \pm 0.08_{\text{sys}}$, consistent with the EGRET (Hartman et al. 1999) and the previously reported three months of LAT detection (Abdo et al. 2009c).
3. Extrapolated to higher energies, the LAT spectrum is barely consistent with the HESS spectrum (Aharonian et al. 2009) only if the HESS spectrum is lowered in flux by its normalization error.
4. A single-zone SSC model can explain all of the multi-wavelength emission from the core except for the non-simultaneous HESS emission. It is not possible to fit the entire SED, including the HESS emission, with a single-zone Compton-scattering model due to internal $\gamma\gamma$ absorption effects.
5. SSC modeling results are consistent with suggestions by Chiaberge et al. that we are seeing γ -rays from a different origin than we would if we were looking down the jet. This could be explained by a spine in sheath (Chiaberge et al. 2000) or decelerating jet scenario (Georganopoulos & Kazanas 2003).

The *Fermi* LAT Collaboration acknowledges generous ongoing support from a number of agencies and institutes that have supported both the development and the operation of the LAT as well as scientific data analysis. These include the National Aeronautics and Space Administration and the Department of Energy in the United States, the Commissariat à l’Energie Atomique and the Centre National de la Recherche Scientifique/

Institut National de Physique Nucléaire et de Physique des Particules in France, the Agenzia Spaziale Italiana and the Istituto Nazionale di Fisica Nucleare in Italy, the Ministry of Education, Culture, Sports, Science and Technology (MEXT), High Energy Accelerator Research Organization (KEK) and Japan Aerospace Exploration Agency (JAXA) in Japan, and the K. A. Wallenberg Foundation, the Swedish Research Council and the Swedish National Space Board in Sweden.

Additional support for science analysis during the operations phase is gratefully acknowledged from the Istituto Nazionale di Astrofisica in Italy and the Centre National d'Études Spatiales in France.

We are grateful to the anonymous referee for useful comments which have improved the manuscript. We thank N. Odegard for providing us with the *WMAP* image and the *Suzaku* team for their calibration and satellite operation. We also acknowledge the *Swift* Team and the *Swift*/XRT monitoring program efforts as well as *Swift* analysis supported by NASA grants NNX08AV77G and NNX09AU07G.

APPENDIX

IT ABSORPTION CONSTRAINT ON THE DOPPLER FACTOR OF CEN A

In the SSC model, the Doppler factor, δ_D , and comoving, tangled, isotropic magnetic field strength, B , may be estimated from the dimensionless peak energy and νF_ν flux, ϵ_{pk} and $f_{\text{pk}}^{\text{syn}}$ of the synchrotron and SSC components, respectively, observed in the SED. Assuming that the comoving blob size can be constrained by $R'_b = t_v \delta_D c / (1+z)$, this gives

$$\delta_D = 1.6 \left(\frac{\epsilon_{\text{pk}}^{\text{SSC}}}{1} \right)^{1/2} \left(\frac{10^{-7}}{\epsilon_{\text{pk}}^{\text{syn}}} \right) \left(\frac{D}{10^{25} \text{ cm}} \right)^{1/2} \left(\frac{1 \text{ day}}{t_v} \right)^{1/2} \times \left(\frac{f_{\text{pk}}^{\text{syn}}}{10^{-10} \text{ erg s}^{-1} \text{ cm}^{-2}} \right)^{1/2} \left(\frac{10^{-10} \text{ erg s}^{-1} \text{ cm}^{-2}}{f_{\text{pk}}^{\text{SSC}}} \right)^{1/4} \quad (\text{A1})$$

$$B = 0.26 \text{ G} \left(\frac{t_v}{1 \text{ day}} \right)^{1/2} \left(\frac{10^{25} \text{ cm}}{D} \right)^{1/2} \left(\frac{\epsilon_{\text{pk}}^{\text{syn}}}{10^{-7}} \right)^3 \left(\frac{1}{\epsilon_{\text{pk}}^{\text{SSC}}} \right)^{3/2} \times \left(\frac{f_{\text{pk}}^{\text{SSC}}}{10^{-10} \text{ erg s}^{-1} \text{ cm}^{-2}} \right)^{1/4} \left(\frac{10^{-10} \text{ erg s}^{-1} \text{ cm}^{-2}}{f_{\text{pk}}^{\text{syn}}} \right)^{1/2} \quad (\text{A2})$$

(Ghisellini et al. 1996), where t_v is the variability timescale and D is the distance to the source. The Doppler factor, $\delta_D = [\Gamma_j(1 - \beta_j \mu)]^{-1}$ where the Bulk Lorentz factor is $\Gamma_j = (1 - \beta_j^2)^{-1/2}$, $\beta_j c$ is the speed of the jet, and $\theta = \cos^{-1} \mu$ is the angle of the jet with respect to our line of sight. In order for γ -rays to escape an emission region, the $\gamma\gamma \rightarrow e^+e^-$ absorption optical depth, $\tau_{\gamma\gamma}$, cannot be too large. Assuming that the νF_ν synchrotron flux, $f_{\epsilon}^{\text{syn}}$, is given by a broken power law, for $\tau_{\gamma\gamma} < 1$ for a photon with dimensionless energy ϵ_γ this implies

$$\delta_D \geq \left[10^3 \times 2^{A-1} (1+z)^{2-2A} \left(\frac{\epsilon_\gamma}{10^7} \right) \left(\frac{D}{10^{25} \text{ cm}} \right)^2 \times \left(\frac{f_{\epsilon}^{\text{syn}}}{10^{-10} \text{ erg s}^{-1} \text{ cm}^{-2}} \right) \left(\frac{1 \text{ day}}{t_v} \right) \right]^{\frac{1}{6-2A}} \quad (\text{A3})$$

(Doni & Ghisellini 1995), where $f_{\epsilon}^{\text{syn}} \propto \epsilon^A$ and A is the index of the synchrotron spectrum below the break for

$$\epsilon_\gamma^{-1} < \frac{(1+z)^2 \epsilon_{\text{brk}}}{2\delta_D}$$

and above the break for

$$\epsilon_\gamma^{-1} > \frac{(1+z)^2 \epsilon_{\text{brk}}}{2\delta_D}.$$

Solving Equation (A1) for t_v and inserting this into Equation (A3), one gets the constraint

$$\delta_D \geq 4.4 \left[2^{1-A} (1+z)^{2-2A} \left(\frac{\epsilon_\gamma}{10^7} \right) \left(\frac{D}{10^{25} \text{ cm}} \right) \times \left(\frac{f_{\epsilon}^{\text{syn}}}{10^{-10} \text{ erg s}^{-1} \text{ cm}^{-2}} \right) \left(\frac{\epsilon_{\text{pk}}^{\text{syn}}}{1 \times 10^{-7}} \right)^2 \left(\frac{1}{\epsilon_{\text{pk}}^{\text{SSC}}} \right) \times \left(\frac{f_{\text{pk}}^{\text{syn}}}{10^{-10} \text{ erg s}^{-1} \text{ cm}^{-2}} \right)^{1/2} \left(\frac{10^{-10} \text{ erg s}^{-1} \text{ cm}^{-2}}{f_{\text{pk}}^{\text{SSC}}} \right) \right]^{1/4}. \quad (\text{A4})$$

For Cen A, $D = 3.7 \text{ Mpc} = 1.1 \times 10^{25} \text{ cm}$ and $z \approx 0$. The spectral parameters can be obtained from the SED of the core of Cen A (see Figure 5): $\epsilon_{\text{pk}}^{\text{syn}} = 1.6 \times 10^{-7}$, $\epsilon_{\text{pk}}^{\text{SSC}} = 0.3$, $f_{\text{pk}}^{\text{syn}} = 3 \times 10^{-10} \text{ erg s}^{-1} \text{ cm}^{-2}$, and $f_{\text{pk}}^{\text{SSC}} = 9 \times 10^{-10} \text{ erg s}^{-1} \text{ cm}^{-2}$. Note that here we assume that the X-ray data is from the jet; see above. Below the break in the synchrotron spectrum, $A \approx 0.5$, and above the break $A \approx -1$. The highest energy photon bin in the HESS spectrum is $\epsilon_\gamma = 8 \times 10^6$, so that $f_{\epsilon}^{\text{syn}} = 2 \times 10^{-10} \text{ erg s}^{-1} \text{ cm}^{-2}$. These values give the constraint

$$\delta_D \geq 5.3$$

which is Equation (1).

REFERENCES

- Abdo, A., et al. (Fermi-LAT collaboration), 2009a, *ApJS*, **183**, 46 (Bright Source List)
 Abdo, A., et al. (Fermi-LAT collaboration), 2009b, *ApJ*, **699**, 31 (Per A)
 Abdo, A., et al. (Fermi-LAT collaboration), 2009c, *ApJ*, **700**, 597 (LAT Bright AGN Sample)
 Abdo, A., et al. (Fermi-LAT collaboration), 2009d, *ApJ*, **707**, 55 (M87)
 Abdo, A. A., et al. 2010a, *ApJS*, **188**, 405 (First year catalog)
 Abdo, A. A., et al. 2010b, *ApJ*, **715**, 429 (First year AGN catalog)
 Abdo, A. A., et al. 2010c, *Science*, **328**, 725 (Cen A lobes)
 Abdo, A. A., et al. 2010d, *ApJ*, submitted (arXiv:1007.1624)
 Abraham, J., et al. 2007, *Science*, **318**, 938
 Abraham, J., et al. 2008, *Astropar. Phys.*, **29**, 188
 Abraham, J., et al. 2009, arXiv:0906.2347
 Acciari, V. A., et al. 2008, *ApJ*, **679**, 397
 Acciari, V. A., et al. 2009a, *Science*, **325**, 444
 Acciari, V. A., et al. 2009b, *ApJ*, **693**, L104
 Aharonian, F., et al. 2006, *Science*, **314**, 1424
 Aharonian, F., et al. 2009, *ApJ*, **695**, L40
 Ajello, M., et al. 2008, *ApJ*, **673**, 96
 Ajello, M., et al. 2009a, *ApJ*, **690**, 367
 Ajello, M., et al. 2009b, *ApJ*, **699**, 603
 Albert, J., et al. 2008, *ApJ*, **685**, L23
 Aliu, E., et al. 2009, *ApJ*, **692**, L29
 Atwood, W. B., et al. 2009, *ApJ*, **697**, 1071
 Begelman, M. C., Fabian, A. C., & Rees, M. J. 2008, *MNRAS*, **384**, L19
 Bloom, S. D., & Marscher, A. P. 1996, *ApJ*, **461**, 657
 Burns, J. O., Feigelson, E. D., & Schreier, E. J. 1983, *ApJ*, **273**, 128

- Burrows, D. N., et al. 2005, *Space Sci. Rev.*, **120**, 165
- Canosa, C. M., Worrall, D. M., Hardcastle, M. J., & Birkinshaw, M. 1999, *MNRAS*, **310**, 30
- Casandjian, J.-M., & Grenier, I.A. 2008, *A&A*, **489**, 849
- Cheung, C. C. 2007, in AIP Conf. Proc. 921, The First GLAST Symposium, ed. S. Ritz, P. Michelson, & C. A. Meegan (Melville, NY: AIP), 325
- Chiaberge, M., Capetti, A., & Celotti, A. 2001, *MNRAS*, **324**, L33
- Chiaberge, M., Celotti, A., Capetti, A., & Ghisellini, G. 2000, *A&A*, **358**, 104
- Condon, J. J., Helou, G., Sanders, D. B., & Soifer, B. T. 1996, *ApJS*, **103**, 81
- Croston, J. H., et al. 2009, *MNRAS*, **395**, 1999
- Deller, A. T., Tingay, S. J., Bailes, M., & West, C. 2007, *PASP*, **119**, 318
- Dermer, C. D., & Razaque, S. 2010, *ApJ*, submitted, arXiv:1004.4249
- Dermer, C. D., Razaque, S., Finke, J. D., & Atoyan, A. 2009, *New J. Phys.*, **11**, 065016
- Dondi, L., & Ghisellini, G. 1995, *MNRAS*, **273**, 583
- Evans, D. A., Kraft, R. P., Worrall, D. M., Hardcastle, M. J., Jones, C., Forman, W. R., & Murray, S. S. 2004, *ApJ*, **612**, 786
- Fanaroff, B. L., & Riley, J. M. 1974, *MNRAS*, **167**, 31P
- Ferrarese, L., Mould, J. R., Stetson, P. B., Tonry, J. L., Blakeslee, J. P., & Ajhar, E. A. 2007, *ApJ*, **654**, 186
- Finke, J. D., Dermer, C. D., & Böttcher, M. 2008, *ApJ*, **686**, 181
- Fukazawa, Y., et al. 2009, *PASJ*, **61**, S17
- Gehrels, N., et al. 2004, *ApJ*, **611**, 1005
- Georganopoulos, M., & Kazanas, D. 2003, *ApJ*, **594**, L27
- Georganopoulos, M., Sambruna, R. M., Kazanas, D., Cillis, A. N., Cheung, C. C., Perlman, E. S., Blundell, K. M., & Davis, D. S. 2008, *ApJ*, **686**, L5
- Ghisellini, G., Maraschi, L., & Dondi, L. 1996, *A&AS*, **120**, 503
- Grindlay, J. E., Helmken, H. F., Brown, R. H., Davis, J., & Allen, L. R. 1975, *ApJ*, **197**, L9
- Hall, R. D., Walraven, G. D., Djuth, F. T., Haymes, R. C., & Meegan, C. A. 1976, *ApJ*, **210**, 631
- Hardcastle, M. J., Cheung, C. C., Feain, I. J., & Stawarz, Ł. 2009, *MNRAS*, **393**, 1041
- Hardcastle, M. J., Worrall, D. M., Kraft, R. P., Forman, W. R., Jones, C., & Murray, S. S. 2003, *ApJ*, **593**, 169
- Hardcastle, M. J., et al. 2007, *ApJ*, **670**, L81
- Hartman, R. C., Kadler, M., & Tueller, J. 2008, *ApJ*, **688**, 852
- Hartman, R. C., et al. 1999, *ApJS*, **123**, 79
- Hillas, A. M. 1984, *ARA&A*, **22**, 425
- Hinshaw, G., et al. 2009, *ApJS*, **180**, 225
- Horiuchi, S., Meier, D. L., Preston, R. A., & Tingay, S. J. 2006, *PASJ*, **58**, 211
- Ishisaki, Y., et al. 2007, *PASJ*, **59**, S113
- Israel, F. P. 1998, *A&AR*, **8**, 237
- Israel, F. P., Raban, D., Booth, R. S., & Rantakyro, F. T. 2008, *A&A*, **483**, 741
- Jones, D. L., et al. 1996, *ApJ*, **466**, L63
- Junkes, N., Haynes, R. F., Harnett, J. I., & Jauncey, D. L. 1993, *A&A*, **269**, 29
- Kachelrieß, M., Ostapchenko, S., & Tomàs, R. 2009, *New J. Phys.*, **11**, 065017
- Kalberla, P. M. W., Burton, W. B., Hartmann, D., Arnal, E. M., Bajaja, E., Morras, R., & Pöppel, W. G. L. 2005, *A&A*, **440**, 775
- Kellermann, K. I., Zensus, J. A., & Cohen, M. H. 1997, *ApJ*, **475**, L93
- Kellermann, K. I., et al. 2004, *ApJ*, **609**, 539
- Kinzer, R. L., et al. 1995, *ApJ*, **449**, 105
- Koyama, K., et al. 2007, *PASJ*, **59**, S23
- Kraft, R. P., Forman, W. R., Jones, C., Murray, S. S., Hardcastle, M. J., & Worrall, D. M. 2002, *ApJ*, **569**, 54
- Landt, H., & Bignall, H. E. 2008, *MNRAS*, **391**, 967
- Landt, H., Padovani, P., Perlman, E. S., & Giommi, P. 2004, *MNRAS*, **351**, 83
- Ledlow, M. J., & Owen, F. N. 1996, *AJ*, **112**, 9
- Lenain, J.-P., Boisson, C., Sol, H., & Katarzyński, K. 2008, *A&A*, **478**, 111
- Lenain, J.-P., Medina, M. C., Boisson, C., Romero, G. E., Sol, H., & Zech, A. 2009, arXiv:0907.2258
- Lister, M. L., et al. 2009, *AJ*, **138**, 1874
- Ma, C., et al. 1998, *AJ*, **116**, 516
- Marcha, M. J. M., Browne, I. W. A., Impey, C. D., & Smith, P. S. 1996, *MNRAS*, **281**, 425
- Marconi, A., Pastorini, G., Pacini, F., Axon, D. J., Capetti, A., Macchetto, D., Koekemoer, A. M., & Schreier, E. J. 2006, *A&A*, **448**, 921
- Marconi, A., Schreier, E. J., Koekemoer, A., Capetti, A., Axon, D., Macchetto, D., & Caon, N. 2000, *ApJ*, **528**, 276
- Markowitz, A., et al. 2007, *ApJ*, **665**, 209
- Mattox, J. R., et al. 1996, *ApJ*, **461**, 396
- Meisenheimer, K., et al. 2007, *A&A*, **471**, 453
- Mitsuda, K., et al. 2007, *PASJ*, **59**, S1
- Morganti, R., Killeen, N. E. B., Ekers, R. D., & Oosterloo, T. A. 1999, *MNRAS*, **307**, 750
- Moskalenko, I. V., Stawarz, Ł., Porter, T. A., & Cheung, C. C. 2009, *ApJ*, **693**, 1261
- Mueller, C., et al. 2009, arXiv:0912.0686
- Mukherjee, R., Halpern, J., Mirabal, N., & Gotthelf, E. V. 2002, *ApJ*, **574**, 693
- Neronov, A., & Aharonian, F. A. 2007, *ApJ*, **671**, 85
- Neumayer, N., Cappellari, M., Reunanen, J., Rix, H.-W., van der Werf, P. P., de Zeeuw, P. T., & Davies, R. I. 2007, *ApJ*, **671**, 1329
- Ojha, R., et al. 2005, *AJ*, **130**, 2529
- Ojha, R., et al. 2009, arXiv:1001.0059
- Piner, B. G., Pant, N., & Edwards, P. G. 2008, *ApJ*, **678**, 64
- Quillen, A. C., de Zeeuw, P. T., Phinney, E. S., & Phillips, T. G. 1992, *ApJ*, **391**, 121
- Rothschild, R. E., et al. 2006, *ApJ*, **641**, 801
- Shepherd, M. C. 1997, in AIP Conf. Ser. 125, Astron. Data Anal. Softw. Syst. VI, ed. G. Hunt & H. E. Payne (San Francisco, CA: ASP), 77
- Silge, J. D., Gebhardt, K., Bergmann, M., & Richstone, D. 2005, *AJ*, **130**, 406
- Sreekumar, P., Bertsch, D. L., Hartman, R. C., Nolan, P. L., & Thompson, D. J. 1999, *Astropart. Phys.*, **11**, 221
- Stawarz, Ł., Aharonian, F., Wagner, S., & Ostrowski, M. 2006, *MNRAS*, **371**, 1705
- Stawarz, Ł., Sikora, M., & Ostrowski, M. 2003, *ApJ*, **597**, 186
- Steinle, H., et al. 1998, *A&A*, **330**, 97
- Strittmatter, P. A., Serkowski, K., Carswell, R., Stein, W. A., Merrill, K. M., & Burbidge, E. M. 1972, *ApJ*, **175**, L7
- Takahashi, T., et al. 2007, *PASJ*, **59**, S35
- Tavecchio, F., Maraschi, L., & Ghisellini, G. 1998, *ApJ*, **509**, 608
- Tingay, S. J., et al. 1998, *AJ*, **115**, 960
- Urry, C. M., & Padovani, P. 1995, *PASP*, **107**, 803
- Weiß, A., Kovács, A., Güsten, R., Menten, K. M., Schuller, F., Siringo, G., & Kreysa, E. 2008, *A&A*, **490**, 77